

MMSE Channel Estimation in Large-Scale MIMO: Improved Robustness with Reduced Complexity

Giacomo Bacci, *Senior Member, IEEE*, Antonio Alberto D'Amico, *Senior Member, IEEE*, and Luca Sanguinetti, *Senior Member, IEEE*

Abstract—Large-scale MIMO systems with a massive number N of individually controlled antennas pose significant challenges for minimum mean square error (MMSE) channel estimation, based on uplink pilots. The major ones arise from the computational complexity, which scales with N^3 , and from the need for accurate knowledge of the channel statistics. This paper aims to address both challenges by introducing reduced-complexity channel estimation methods that achieve the performance of MMSE in terms of estimation accuracy and uplink spectral efficiency while demonstrating improved robustness in practical scenarios where channel statistics must be estimated. This is achieved by exploiting the inherent structure of the spatial correlation matrix induced by the array geometry. Specifically, we use a Kronecker decomposition for uniform planar arrays and a well-suited circulant approximation for uniform linear arrays. By doing so, a significantly lower computational complexity is achieved, scaling as $N\sqrt{N}$ and $N \log N$ for squared planar arrays and linear arrays, respectively.

Index Terms—Large-scale MIMO, channel estimation, Kronecker decomposition, circulant matrix, uniform planar arrays, covariance matrix estimation.

I. INTRODUCTION AND MOTIVATION

Communications theorists are always looking for new technologies to improve the speed and reliability of wireless communications. Among these technologies, the multiple antenna technology has made significant advances, with the latest implementation being massive multiple-input multiple-output (MIMO) [2], introduced with the advent of 5G [3]. Researchers are now exploring improved deployment methods for massive MIMO, incorporating more antennas and optimized signal processing algorithms to take advantage of its potential benefits. This evolution of massive MIMO has been referred to as massive MIMO 2.0 [4], leading to the exploration of MIMO systems with extremely larger antenna arrays. This is referred to as X-MIMO in industry terminology. Various terms, such as extremely large aperture arrays (ELAAs) [3], extremely large-scale MIMO (XL-MIMO) [5], and ultra-massive MIMO (UM-

MIMO) [6], have also been suggested in academic literature. In this paper, we simply use the large-scale MIMO terminology.

Accurate channel state information (CSI) is crucial for the efficient use of large-scale MIMO, enabling precise transmission beamforming in downlink (DL) and coherent signal combining in uplink (UL). The basic way to acquire CSI in time-division duplexing systems is to transmit a predefined pilot sequence and estimate the channel coefficients at the base station (BS). However, performing minimum mean square error (MMSE) channel estimation in a large-scale MIMO system with a massive number N of independent radio-frequency (RF) chains (e.g., in the order of thousands) poses critical challenges in the implementation of the MMSE estimator (whose computational complexity may scale as N^3 due to matrix inversion, e.g., [7], [8]) and in the acquisition of the channel statistics, i.e., the spatial correlation matrices. In practical communication scenarios, the latter are not known a priori and must be estimated based on observed channel measurements [2]. This is crucial for designing robust and efficient large-scale MIMO systems [4]. An alternative is to use the least-squares (LS) estimator [9], which requires neither matrix inversion nor statistical information. However, its performance is significantly inferior to MMSE, e.g., [2]. The objective of this paper is to tackle this challenge by developing channel estimation schemes that achieve accuracy levels comparable to the MMSE estimator, while also offering reduced complexity and enhanced robustness to the imperfect knowledge of channel statistics.

A. Related work

A variety of schemes exists in the literature to achieve the same performance of MMSE while handling complexity that scales with the number of antennas. These include, for example, methods based on exhaustive search [10], hierarchical search [11]–[13], compressed sensing (CS) [14]–[16], and tensor decomposition [17]–[19]. The exhaustive method in [10] exploits a sequence of training symbols, whose overhead becomes prohibitively high as the number N of antennas increases. To overcome this issue, a hierarchical search based on a predefined codebook is proposed in [11]–[13]. However, while significantly reducing the complexity, the limited codebook size severely affects the estimation accuracy. Alternative methods to reduce the pilot overhead take advantage of CS techniques, which exploit the fact that the propagation channels of most practical communication scenarios can be sparsely represented in the angular domain.

A preliminary version of this article can be found in [1].

Manuscript received 3 April 2024; revised 2 August 2024; accepted 25 September 2024. Date of publication XX MONTH 202Y; date of current version XX MONTH 202Y. The associate editor coordinating the review of this article and approving it for publication was W. Cheng. (*Corresponding author: Giacomo Bacci.*)

G. Bacci, A.A. D'Amico and L. Sanguinetti are with the Dipartimento di Ingegneria dell'Informazione, University of Pisa, 56122, Pisa, Italy (email: giacomo.bacci@unipi.it, antonio.damico@unipi.it, luca.sanguinetti@unipi.it). They are partially supported by the Italian Ministry of Education and Research (MUR) in the framework of the FoReLab project (Departments of Excellence).

Color versions of one or more figures in this article are available at <https://doi.org/10.1109/TWC.2024.3470124>.

Digital Object Identifier 10.1109/TWC.2024.3470124

A parametric approach is used in [16] for line-of-sight (LoS) communications. A different approach is pursued in [20], which exploits the high rank deficiency observed in the spatial correlation matrices caused by the large-scale MIMO geometry [21] to derive a subspace-based channel estimation approach. The complexity saving is due to a compact eigenvalue decomposition, which allows the proposed reduced-subspace LS (RS-LS) estimator to attain the MMSE performance when the pilot signal-to-noise ratio (SNR) becomes significantly large. However, this might not hold true, especially for practical transmitter-receiver distances.

The vast majority of the aforementioned literature assumes that the channel statistics are perfectly known. However, this assumption is questionable because the matrix dimensions grow with N and the statistics change over time (e.g., due to mobility). Practical covariance estimates are imperfect because the number of observations may be comparable to N . One promising approach to estimating a large-dimensional covariance matrix with a small number of observations is to regularize the sample covariance matrix [2], [22]. This makes it scenario-dependent.

B. Main contributions

This paper focuses on the development of channel estimation schemes that, compared to the optimal MMSE estimator, offer both lower computational complexity and improved robustness in the presence of imperfect knowledge of channel statistics. This is accomplished by exploiting the inherent structure of the spatial correlation matrix shaped by the array geometry, which is known in a given deployment scenario. For a uniform planar array (UPA), we use the Kronecker product decomposition [23], [24] to effectively separate the horizontal and vertical components within the array. For a uniform linear array (ULA), we use an appropriate circulant approximation [25]–[27], which allows the application of the discrete Fourier transform (DFT). Numerical results are used to evaluate the effectiveness of the proposed methods in terms of normalized mean square estimation error (NMSE) and spectral efficiency (SE) in the uplink with different combining schemes. The results show that the proposed schemes achieve performance levels comparable to those with the MMSE estimator, while significantly reducing computational complexity. Specifically, the overall computational load, including the estimation of the spatial correlation matrices, scales as $N\sqrt{N}$ and $N \log N$ for squared planar arrays and linear arrays, respectively. Moreover, the schemes exhibit improved robustness in scenarios with imperfect knowledge of channel statistics, making them more suitable for dynamic environments. Remarkably, this is achieved without any regularization factor, making the schemes applicable without the need for fine-tuning according to the specific scenarios.

C. Paper outline and notation

The remainder of the paper is structured as follows. Sect. II presents the system and channel models, whereas Sect. III revises the channel estimation problem in the presence of perfect knowledge of the channel statistics. Sects. IV and V

derive low-complexity schemes for UPA and ULA scenarios, respectively. Sect. VI addresses the problem of estimating the channel statistics. Sects. VII and VIII investigate the complexity and the performance of the proposed schemes in terms of achievable uplink SE. Sect. IX concludes the paper.

Matrices and vectors are denoted by boldface uppercase and lowercase letters, respectively. The notation $[\mathbf{A}]_{i,k}$ is used to indicate the (i, k) th entry of the enclosed matrix \mathbf{A} , and $\mathbf{A} = \text{diag}(a(n); n = 1, \dots, N)$ denotes an $N \times N$ diagonal matrix with entries $a(n)$ along its main diagonal. $\|\mathbf{x}\|$ denotes the Euclidean norm of vector \mathbf{x} , and $\|\mathbf{A}\|_F$ denotes the Frobenius norm of matrix \mathbf{A} . Trace and rank of a matrix \mathbf{A} are denoted by $\text{tr}(\mathbf{A})$ and $\text{rank}(\mathbf{A})$, respectively, whereas \mathbf{A}^T and \mathbf{A}^H are the transpose and the conjugate transpose of \mathbf{A} , respectively, and j denotes the imaginary unit. The $N \times N$ identity matrix and the all-zero vector with N elements are denoted by \mathbf{I}_N and $\mathbf{0}_N$, respectively. We use $\delta(\cdot)$ to denote the Dirac delta function, $\text{mod}(\cdot, \cdot)$ to denote the modulus operation, $\lfloor \cdot \rfloor$ to truncate the argument, \otimes to indicate the Kronecker product, and $\Re(\cdot)$ to represent the real part of a complex number.

D. Reproducible research

The MATLAB code used to obtain the simulation results will be made available to the interested readers upon request.

II. SYSTEM AND CHANNEL MODEL

We consider a large-scale MIMO system with K active user equipments (UEs). The BS is equipped with a UPA located in the yz plane, and consisting of N independent RF chains, arranged into N_V rows, each hosting N_H antennas: $N = N_H N_V$.¹ As illustrated in Fig. 1, the inter-element spacing across horizontal and vertical directions is Δ_H and Δ_V , respectively [28, Fig. 1]. The location of the n th antenna, with $1 \leq n \leq N$, with respect to the origin is $\mathbf{u}_n = [0, i(n)\Delta_H, j(n)\Delta_V]^T$, where $i(n) = \text{mod}(n-1, N_H)$ and $j(n) = \lfloor (n-1)/N_H \rfloor$ are the horizontal and vertical indices of element n .

We call $\mathbf{h}_k \in \mathbb{C}^N$ the channel vector between the single-antenna UE k and the BS, and model it as [29]

$$\mathbf{h}_k = \iint_{-\pi/2}^{\pi/2} g_k(\varphi, \theta) \mathbf{a}(\varphi, \theta) d\varphi d\theta \quad (1)$$

where $\mathbf{a}(\varphi, \theta)$ is the array response vector [2, Sect. 7.3]

$$\mathbf{a}(\varphi, \theta) = \left[e^{j\mathbf{k}(\varphi, \theta)^T \mathbf{u}_1}, \dots, e^{j\mathbf{k}(\varphi, \theta)^T \mathbf{u}_N} \right]^T \quad (2)$$

of the UPA from azimuth angle φ and elevation angle θ , and $\mathbf{k}(\varphi, \theta) = \frac{2\pi}{\lambda} [\cos(\theta) \cos(\varphi), \cos(\theta) \sin(\varphi), \sin(\theta)]^T$ is the wave vector at wavelength λ . Also, $g_k(\varphi, \theta)$ is the *angular spreading function* [2, Sect. 2.6], which accounts for the local scattering model [30, Chap. 7].

We consider the conventional block-fading model, where the channel \mathbf{h}_k is constant within one time-frequency block

¹The analysis is valid for any orientation of the UPA with respect to the reference system, and includes both horizontal and vertical ULAs, by setting $N_V = 1$ and $N_H = 1$, respectively.

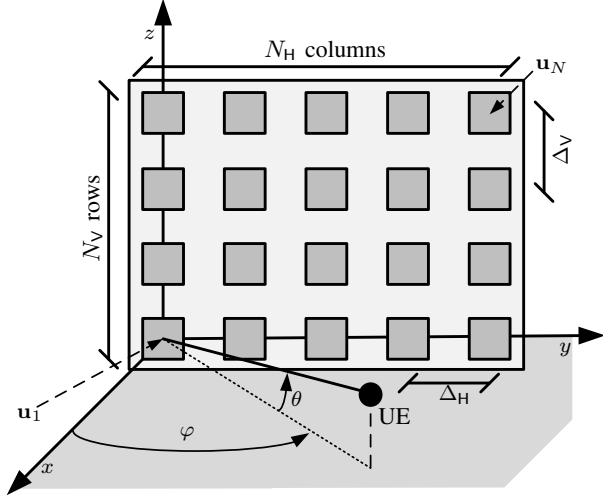


Fig. 1. Diagram of the UPA located in the yz -plane, with a planar wave impinging with elevation θ and azimuth φ .

and takes independent realizations across blocks from a stationary stochastic distribution. In accordance with [29], we model $g_k(\varphi, \theta)$ as a spatially uncorrelated circularly symmetric Gaussian stochastic process with cross-correlation

$$\mathbb{E}\{g_k(\varphi, \theta)g_k^*(\varphi', \theta')\} = \beta_k f_k(\varphi, \theta)\delta(\varphi - \varphi')\delta(\theta - \theta') \quad (3)$$

where β_k is the average channel gain and $f_k(\varphi, \theta)$ is the normalized *spatial scattering function* [29] such that $\iint f_k(\varphi, \theta)d\theta d\varphi = 1$. By using (2), the elements of $\mathbf{R}_k = \mathbb{E}\{\mathbf{h}_k\mathbf{h}_k^H\}$ are computed as [2, Sect. 7.3.2]

$$[\mathbf{R}_k]_{m,l} = \beta_k \iint_{-\pi/2}^{\pi/2} e^{jk(\varphi, \theta)^T(\mathbf{u}_m - \mathbf{u}_l)} f_k(\varphi, \theta) d\varphi d\theta. \quad (4)$$

In particular, the elements of \mathbf{R}_k are affected by the 3D local scattering model, that determines the typical values for azimuth and elevation angles, and their respective angular spreads σ_φ and σ_θ . Measurements indicate that the range of interest for both azimuth and elevation angular spreads in typical cellular scenarios is given by $[5^\circ, 15^\circ]$, e.g., [31].

III. CHANNEL ESTIMATION

We assume that channel estimation is performed by using orthogonal pilot sequences of length $\tau_p \geq K$. We call $\phi_k \in \mathbb{C}^{\tau_p}$ the pilot sequence used by UE k and assume $|\phi_k[i]|^2 = 1$, so that $\phi_k^H \phi_k = \tau_p$. In the absence of pilot contamination, the observation vector is [2, Sect. 3]

$$\mathbf{y}_k = \tau_p \sqrt{\rho} \mathbf{h}_k + \mathbf{w} \quad (5)$$

where ρ is the transmit power and $\mathbf{w} \sim \mathcal{CN}(\mathbf{0}_N, \tau_p \sigma^2 \mathbf{I}_N)$.

An arbitrary *linear* estimator of \mathbf{h}_k based on \mathbf{y}_k takes the form [2, Sect. 3]

$$\hat{\mathbf{h}}_k = \mathbf{A}_k \mathbf{y}_k \quad (6)$$

for some deterministic matrix $\mathbf{A}_k \in \mathbb{C}^{N \times N}$ that specifies the estimation scheme. The NMSE of the estimation error $\tilde{\mathbf{h}}_k \triangleq \mathbf{h}_k - \hat{\mathbf{h}}_k$ can be computed as

$$\text{NMSE} = 1 - \frac{2\sqrt{\rho}\tau_p \Re(\text{tr}(\mathbf{R}_k \mathbf{A}_k)) + \rho\tau_p^2 \text{tr}(\mathbf{A}_k \mathbf{Q}_k \mathbf{A}_k^H)}{\text{tr}(\mathbf{R}_k)} \quad (7)$$

where

$$\mathbf{Q}_k = \frac{1}{\rho\tau_p^2} \mathbb{E}\{\mathbf{y}_k \mathbf{y}_k^H\} = \mathbf{R}_k + \frac{1}{\gamma} \mathbf{I}_N \quad (8)$$

with $\gamma = \tau_p \rho / \sigma^2$ being the transmit SNR (i.e., measured at the UE side), during the channel estimation phase.

A. MMSE and LS estimators

The scheme that minimizes (7) is the MMSE estimator, according to which

$$\mathbf{A}_k^{\text{MMSE}} = \frac{1}{\tau_p \sqrt{\rho}} \mathbf{R}_k \mathbf{Q}_k^{-1}. \quad (9)$$

The MMSE estimator is optimal but requires the following operations:

- 1) Estimation of the spatial covariance matrix \mathbf{R}_k ;
- 2) Computation of the inverse of \mathbf{Q}_k ;
- 3) Computation of the channel estimate

$$\hat{\mathbf{h}}_k^{\text{MMSE}} = \mathbf{A}_k^{\text{MMSE}} \mathbf{y}_k. \quad (10)$$

The main computational cost comes from the inversion of \mathbf{Q}_k , which scales as $\mathcal{O}(N^3)$ if structural properties of the matrix are not exploited. Therefore, an intense computational effort is required when N is large, as envisioned in large-scale MIMO [6].

An alternative is the LS estimator with

$$\mathbf{A}_k^{\text{LS}} = \frac{1}{\tau_p \sqrt{\rho}} \mathbf{I}_N \quad (11)$$

which uses no prior information on the channel statistics and array geometry. Unlike the MMSE estimator, its computational complexity is $\mathcal{O}(N)$, due to the multiplication between the diagonal matrix \mathbf{A}_k^{LS} and \mathbf{y}_k . However, this efficiency comes at the cost of reduced accuracy.

B. MMSE estimators for low and rich scattering

Two estimators for low and rich scattering scenarios are described below. Both take advantage of the array geometry, but apply to two different channel propagation conditions. The first one assumes that propagation takes place in a LoS scenario with a single plane-wave arriving from θ_k and φ_k . Under this hypothesis, $\mathbf{h}_k = g_k(\varphi_k, \theta_k) \mathbf{a}(\varphi_k, \theta_k)$ and $\mathbf{R}_k^{\text{LoS}} = \beta_k \mathbf{a}(\varphi_k, \theta_k) \mathbf{a}(\varphi_k, \theta_k)^H$. Replacing \mathbf{R}_k with $\mathbf{R}_k^{\text{LoS}}$ into (9) yields $\hat{\mathbf{h}}_k^{\text{LoS}} = \mathbf{A}_k^{\text{LoS}} \mathbf{y}_k$, where

$$\mathbf{A}_k^{\text{LoS}} = \frac{1}{\tau_p \sqrt{\rho}} \frac{\beta_k \gamma}{1 + N\beta_k \gamma} \mathbf{a}(\varphi_k, \theta_k) \mathbf{a}(\varphi_k, \theta_k)^H \quad (12)$$

whose complexity is $\mathcal{C}_{\text{LoS}} = \mathcal{O}(N)$, due to the evaluation of the product between $\mathbf{A}_k^{\text{LoS}}$ in (12) and \mathbf{y}_k (no pre-computation phase is required). However, the LoS-based estimator works well only when the channel vector is generated by a single plane-wave arriving from (φ_k, θ_k) , whose knowledge must be perfect at the BS.

Conversely, when the propagation scenario is highly scattered, and planar waves arrive uniformly within the angular domain in front of the UPA, we can make use of the isotropic (ISO) approximation proposed in [20]. According to [20],

$\mathbf{R}_k^{\text{ISO}} = \overline{\mathbf{U}} \overline{\mathbf{\Lambda}} \overline{\mathbf{U}}^{\text{H}}$, where $\overline{\mathbf{U}}$ is the (reduced-order) eigenvector matrix corresponding to the non-zero eigenvalues in $\overline{\mathbf{\Lambda}}$, obtained through the *compact* eigenvalue decomposition of $\mathbf{R}_k^{\text{ISO}}$ whose (m, l) th entry is

$$[\mathbf{R}_k^{\text{ISO}}]_{m,l} = \text{sinc} \left(2\sqrt{\delta_{\text{H},ml}^2 + \delta_{\text{V},ml}^2} \right) \quad (13)$$

with

$$\delta_{\text{H},ml} = [i(m) - i(l)] \Delta_{\text{H}}/\lambda \quad (14)$$

$$\delta_{\text{V},ml} = [j(m) - j(l)] \Delta_{\text{V}}/\lambda \quad (15)$$

and $\text{sinc}(x) = \sin(\pi x)/(\pi x)$ [28]. Approximating $\mathbf{R}_k^{\text{ISO}}$ with $\tilde{\mathbf{R}}_k^{\text{ISO}} = \overline{\mathbf{U}} \overline{\mathbf{U}}^{\text{H}}$, and replacing \mathbf{R}_k with $\tilde{\mathbf{R}}_k^{\text{ISO}}$ into (9) yields $\hat{\mathbf{h}}_k^{\text{ISO}} = \mathbf{A}_k^{\text{ISO}} \mathbf{y}_k$ [20, Eq. (18)], with

$$\mathbf{A}_k^{\text{ISO}} = \frac{1}{\tau_p \sqrt{\rho}} \overline{\mathbf{U}} \overline{\mathbf{U}}^{\text{H}}. \quad (16)$$

The main advantage of (16) is that no matrix estimation and inversion is required, since $\overline{\mathbf{U}}$ is known and does not depend on UE k . Therefore, it can be used to precompute and store $\overline{\mathbf{U}} \overline{\mathbf{U}}^{\text{H}}$. Accordingly, the complexity of $\hat{\mathbf{h}}_k^{\text{ISO}}$ is only due to the matrix-vector product computation between $\mathbf{A}_k^{\text{ISO}}$ and \mathbf{y}_k , and is $\mathcal{C}_{\text{ISO}} = \mathcal{O}(N^2)$.

IV. REDUCED-COMPLEXITY METHOD FOR UPA

We first consider a UPA and develop a channel estimator that exploits the array geometry and makes use of a Kronecker product approximation of \mathbf{R}_k , in the form

$$\mathbf{R}_k \approx \mathbf{K}_1 \otimes \mathbf{K}_2 \quad (17)$$

where $\mathbf{K}_1 \in \mathbb{C}^{N_{\text{V}} \times N_{\text{V}}}$ and $\mathbf{K}_2 \in \mathbb{C}^{N_{\text{H}} \times N_{\text{H}}}$ are suitable matrices. The main advantage of using (17) is the computational savings in calculating $\mathbf{R}_k \mathbf{Q}_k^{-1}$. In fact, replacing \mathbf{R}_k with $\mathbf{K}_1 \otimes \mathbf{K}_2$ leads to the following approximation of $\mathbf{A}_k^{\text{MMSE}}$ in (9):

$$\begin{aligned} \mathbf{A}_k^{\text{MMSE}} &\approx \mathbf{A}_k^{\text{Kron}} = \frac{1}{\tau_p \sqrt{\rho}} (\mathbf{U}_1 \otimes \mathbf{U}_2) (\mathbf{\Lambda}_1 \otimes \mathbf{\Lambda}_2) \\ &\times \left(\mathbf{\Lambda}_1 \otimes \mathbf{\Lambda}_2 + \frac{1}{\gamma} \mathbf{I}_N \right)^{-1} \left(\mathbf{U}_1^{\text{H}} \otimes \mathbf{U}_2^{\text{H}} \right) \end{aligned} \quad (18)$$

where \mathbf{U}_1 (\mathbf{U}_2 , respectively) and $\mathbf{\Lambda}_1$ ($\mathbf{\Lambda}_2$, respectively) are the eigenvector and eigenvalue matrices obtained by the spectral decomposition of \mathbf{K}_1 (\mathbf{K}_2 , respectively), i.e., $\mathbf{K}_1 = \mathbf{U}_1 \mathbf{\Lambda}_1 \mathbf{U}_1^{\text{H}}$ and $\mathbf{K}_2 = \mathbf{U}_2 \mathbf{\Lambda}_2 \mathbf{U}_2^{\text{H}}$. Compared to the spectral decomposition of \mathbf{R}_k or the inversion of \mathbf{Q}_k , the spectral decomposition of \mathbf{K}_1 and \mathbf{K}_2 requires much fewer operations, as will be discussed in Sect. VII.

A. Kronecker-based approximation

We begin by rewriting (4) as

$$\mathbf{R}_k = \beta_k \iint_{-\pi/2}^{\pi/2} f_k(\varphi, \theta) \mathbf{B}_{\text{V}}(\theta) \otimes \mathbf{B}_{\text{H}}(\varphi, \theta) d\varphi d\theta, \quad (19)$$

where $\mathbf{B}_{\text{H}}(\varphi, \theta) \in \mathbb{C}^{N_{\text{H}} \times N_{\text{H}}}$ and $\mathbf{B}_{\text{V}}(\theta) \in \mathbb{C}^{N_{\text{V}} \times N_{\text{V}}}$ are Hermitian Toeplitz matrices given by

$$[\mathbf{B}_{\text{H}}(\varphi, \theta)]_{m,l} = e^{j2\pi(\Delta_{\text{H}}/\lambda)[i(m)-i(l)] \sin \varphi \cos \theta}, \quad (20)$$

$$[\mathbf{B}_{\text{V}}(\theta)]_{m,l} = e^{j2\pi(\Delta_{\text{V}}/\lambda)[j(m)-j(l)] \sin \theta}. \quad (21)$$

Computing the integral (19) with respect to φ yields

$$\mathbf{R}_k = \beta_k \int_{-\pi/2}^{\pi/2} \mathbf{B}_{\text{V}}(\theta) \otimes \tilde{\mathbf{R}}_{\text{H},k}(\theta) d\theta \quad (22)$$

where

$$\tilde{\mathbf{R}}_{\text{H},k}(\theta) = \int_{-\pi/2}^{\pi/2} f_k(\varphi, \theta) \mathbf{B}_{\text{H}}(\varphi, \theta) d\varphi. \quad (23)$$

In general, the integral expression of \mathbf{R}_k given in (22) cannot be simplified as a Kronecker product of two matrices. However, in the specific case where all the plane waves are impinging from the same elevation angle $\bar{\theta}$, i.e., when $f_k(\varphi, \theta) = f_k(\varphi) \delta(\theta - \bar{\theta})$ (which means no angular spread across the elevation angle), we have

$$\mathbf{R}_k = \tilde{\mathbf{R}}_{\text{V},k}(\bar{\theta}) \otimes \tilde{\mathbf{R}}_{\text{H},k}(\bar{\theta}) \quad (24)$$

where

$$\tilde{\mathbf{R}}_{\text{H},k}(\bar{\theta}) = \int_{-\pi/2}^{\pi/2} \tilde{f}_k(\varphi) \mathbf{B}_{\text{H}}(\varphi, \bar{\theta}) d\varphi \quad (25)$$

$$\tilde{\mathbf{R}}_{\text{V},k}(\bar{\theta}) = \beta_k \mathbf{B}_{\text{V}}(\bar{\theta}). \quad (26)$$

Note that the representation of \mathbf{R}_k in (24) is not unique. Indeed, taking $\mathbf{R}_{\text{H},k} = \alpha \tilde{\mathbf{R}}_{\text{H},k}(\bar{\theta})$ and $\mathbf{R}_{\text{V},k} = \alpha^{-1} \tilde{\mathbf{R}}_{\text{V},k}(\bar{\theta})$, we have $\mathbf{R}_k = \mathbf{R}_{\text{H},k} \otimes \mathbf{R}_{\text{V},k}$ for any $\alpha \in \mathbb{C}$. We select

$$\mathbf{R}_{\text{H},k} = [\mathbf{R}_k]_{1:1:N_{\text{H}},1:1:N_{\text{H}}} \quad (27)$$

$$\mathbf{R}_{\text{V},k} = [\mathbf{R}_k]_{1:N_{\text{H}},1:N_{\text{H}},1:N_{\text{V}},1:N_{\text{V}}} / [\mathbf{R}_k]_{1,1} \quad (28)$$

where we have adopted the well-known ‘‘colon notation’’ used by MATLAB. In the remainder of this paper, the Kronecker decomposition of \mathbf{R}_k by $\mathbf{R}_{\text{H},k}$ and $\mathbf{R}_{\text{V},k}$ will be referred to as the Kronecker-based approximation (KBA) of the covariance matrix. The Kronecker product of (27) and (28) provides an *exact* representation of \mathbf{R}_k only when $\sigma_{\theta} = 0^\circ$. To assess its robustness for $\sigma_{\theta} > 0^\circ$, Fig. 2(a) shows the normalized squared approximation error (NSAE), defined as

$$\text{NSAE}_{\text{R}} = \frac{\|\mathbf{R}_k - \mathbf{R}_{\text{V},k} \otimes \mathbf{R}_{\text{H},k}\|_{\text{F}}^2}{\|\mathbf{R}_k\|_{\text{F}}^2} \quad (29)$$

as a function of σ_{θ} . We consider a UPA with $N_{\text{H}} = N_{\text{V}} = 16$ elements, using $\Delta_{\text{H}} = \Delta_{\text{V}} = \lambda/2$ at 3 GHz² and assume an azimuth angle $\bar{\varphi} = 0^\circ$ with angular spread $\sigma_{\varphi} = 10^\circ$. Both azimuth and elevation angles follow a Gaussian distribution. For simplicity, we assume $\beta_k = 1$. Two different values of $\bar{\theta}$ are considered: $\bar{\theta} = 0^\circ$ and $\bar{\theta} = \pm 60^\circ$. As expected, the approximation worsens as σ_{θ} increases. Furthermore, the NSAE increases as $|\bar{\theta}|$ increases, owing to the reduced UPA directivity (and hence larger fluctuations in the KBA), and, albeit not reported here for the sake of brevity, it also increases as the UPA size increases (due to a larger size of the covariance matrix \mathbf{R}_k , which impacts the accuracy of the approximation).

²Note that, at this carrier frequency, the propagation occurs in the far-field regime [32].

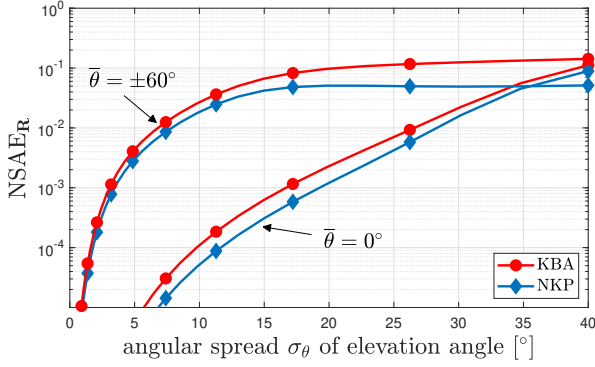
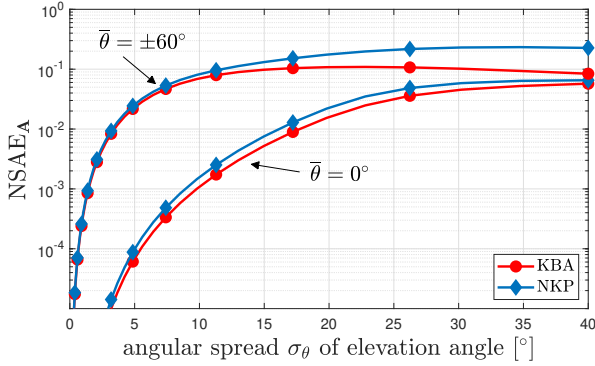
(a) NSAE_R in (29).(b) NSAE_A in (31).

Fig. 2. NSAE of the correlation matrix as a function of the elevation angular spread for KBA and NKP. We consider a UPA with $N_H = N_V = 16$ elements, using $\Delta_H = \Delta_V = \lambda/2$ at 3 GHz. The azimuth angle is $\bar{\varphi} = 0^\circ$ with angular spread $\sigma_\varphi = 10^\circ$. Both azimuth and elevation angles follow a Gaussian distribution.

In Fig. 2(a), comparisons are made with the *nearest Kronecker product* (NKP), derived in [23] by minimizing the NSAE. According to NKP, the matrix \mathbf{R}_k is approximated by $\mathbf{R}_{V,k}^* \otimes \mathbf{R}_{H,k}^*$, where $\mathbf{R}_{H,k}^*$ and $\mathbf{R}_{V,k}^*$ are obtained as

$$(\mathbf{R}_{H,k}^*, \mathbf{R}_{V,k}^*) = \arg \min_{(\mathbf{X}, \mathbf{Y})} \|\mathbf{R}_k - \mathbf{Y} \otimes \mathbf{X}\|_F^2. \quad (30)$$

The NKP solution can be found following the steps detailed in [24]. From Fig. 2(a), we see that the difference between NKP and KBA is relatively small for all the considered values of σ_θ . Notice that, despite (30) is the solution that best approximates \mathbf{R}_k , KBA performs better than NKP as far as the approximation of $\mathbf{A}_k^{\text{MMSE}}$ in (9) is concerned. This can be appreciated with the help of Fig. 2(b), which reports

$$\text{NSAE}_A = \frac{\|\mathbf{A}_k^{\text{MMSE}} - \mathbf{A}_k\|_F^2}{\|\mathbf{A}_k^{\text{MMSE}}\|_F^2} \quad (31)$$

as a function of σ_θ for $\gamma = 10$ dB. The matrix \mathbf{A}_k in (31) is obtained from (9) by replacing \mathbf{R}_k with either $\mathbf{R}_{V,k} \otimes \mathbf{R}_{H,k}$ (KBA curves) or $\mathbf{R}_{V,k}^* \otimes \mathbf{R}_{H,k}^*$ (NKP curves). We see that KBA yields a lower NSAE_A, which results in a superior estimation accuracy when implementing (6), as shown in the next section.

Table I
UPA PARAMETERS.

Parameter	Value
Carrier frequency	$f_0 = 3$ GHz
Wavelength	$\lambda = 10$ cm
Vertical inter-element spacing	$\Delta_V = \lambda/2 = 5$ cm
Horizontal inter-element spacing	$\Delta_H = \lambda/2 = 5$ cm
Height	$b = 10$ m

B. NMSE evaluation

Consider a square UPA with $N_H = N_V = \sqrt{N}$ and all the other relevant parameters listed in Table I. Fig. 3 shows the NMSE in (7) as a function of $N = N_H N_V$. The matrix \mathbf{A}_k in (7) depends on the specific channel estimation scheme. We consider MMSE, LS, LoS, ISO, and the approximate MMSE based on KBA. We evaluate the average NMSE for a UE randomly placed in the simulation setup detailed in Table II, in which the received SNR is $\beta_k \tau_p \rho / \sigma^2$. The path loss β_k is computed following [2, Sect. 2], i.e.,

$$\beta_k = -148.1 \text{ dB} - 37.6 \log_{10} \left(\frac{d_k}{1 \text{ km}} \right) \quad [\text{dB}] \quad (32)$$

where d_k is the distance of UE k from the BS. It is worth noting that, in the considered network setup, in which the UEs are uniformly randomly placed with distances in $[\underline{d}, \bar{d}]$, the probability density function (pdf) of the elevation angle θ is

$$f_{\bar{\theta}}(\theta) = \frac{2b^2}{(\bar{d}^2 - \underline{d}^2) \sin^2 \theta |\tan \theta|}, \quad (33)$$

where b is the BS height on the azimuth plane. Accordingly, small values of $|\theta|$ are much more likely to occur than large values.

The results of Fig. 3 show that the accuracy of the KBA-based estimator attains that of the optimal MMSE, irrespective of the size N . This happens despite the error in the approximation of \mathbf{R}_k , because, as can be deduced from the numerical values in Fig. 2 and (33), the NSAEs (29) and (31) are small enough to guarantee that $\mathbf{A}_k^{\text{Kron}} \mathbf{y}_k$ yields approximately the same NMSE (7) as $\mathbf{A}_k^{\text{MMSE}} \mathbf{y}_k$. The accuracy of the NKP-based estimator, not reported in Fig. 3, overlaps both the MMSE and the KBA ones for the same reason. Similar results can be obtained with a UPA with a rectangular shape.

The impact of the angular spread σ_θ is evaluated in Fig. 4. The same simulation setup of Fig. 3 is considered. Also, we assume $N_H = N_V = 16$ and set $\sigma_\varphi = 10^\circ$. The results show that the KBA-based estimator achieves the best accuracy, with a negligible gap with respect to the MMSE estimator in the range of interest for typical cellular scenarios $[5^\circ, 15^\circ]$, as discussed at the end of Sect. II. For $10^\circ \leq \sigma_\theta \leq 40^\circ$, the difference between KBA and NKP increases, thus confirming the findings of Fig. 2. A similar behavior can be observed using different values for the azimuth angular spread σ_φ .

³The same simulation setup using a Laplacian distribution provide very similar results, not reported here for the sake of brevity.

Table II
SIMULATION PARAMETERS.

Parameter	Value
Minimum distance from UPA \underline{d}	5 m
Maximum distance from UPA \overline{d}	100 m
Azimuth range φ	$[-60^\circ, +60^\circ]$
Azimuth spreading σ_φ	10°
Elevation range θ	$[-63.4^\circ, -5.7^\circ]$
Elevation spreading σ_θ	10°
Azimuth/elevation scattering distribution	Gaussian ³
Path loss reference distance	1 km
Channel gain at reference distance	-148.1 dB
Path loss exponent	3.76
Communication bandwidth B	100 MHz
Transmit power ρ	20 dBm
Noise power	-87 dBm
Length of pilot sequence τ_p	10
Length of coherence block τ_c	200

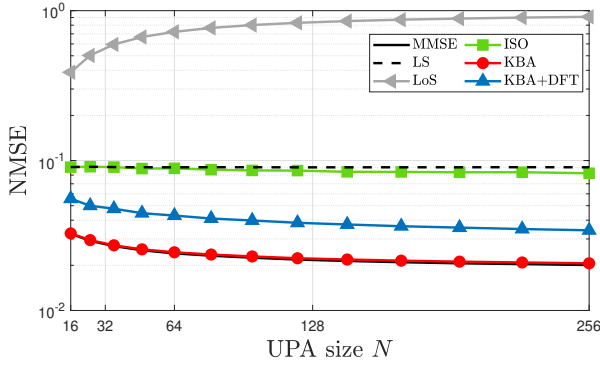


Fig. 3. NMSE for a square UPA with $N_H = N_V = \sqrt{N}$. The UPA parameters are reported in Table I. The simulation parameters are those of Table II.

V. REDUCED-COMPLEXITY METHODS FOR ULA

The UPA model introduced in Sect. II is general enough to encompass both vertical and horizontal configurations, obtained by either $N_H = 1$ or $N_V = 1$, respectively. In those cases, the KBA-based approach has exactly the same complexity of the optimal MMSE one. This is due to the fact that, when N_H (respectively, N_V) is equal to 1, based on (27) [respectively, (28)], the matrix $\mathbf{R}_{H,k}(\bar{\theta})$ [respectively, $\mathbf{R}_{V,k}(\bar{\theta})$] is *exactly* the scalar 1, and hence $\mathbf{R}_k = \mathbf{R}_{V,k}(\bar{\theta})$ [respectively, $\mathbf{R}_k = \mathbf{R}_{H,k}(\bar{\theta})$]. For this reason, not only the complexity, but also the channel estimation performance of the KBA-based method coincides with the MMSE one.

In this section, we develop a channel estimation scheme for a horizontal ULA (i.e., $N = N_H$) that exploits the correlation induced by the array geometry and propagation conditions to approach MMSE performance, while having a computational complexity that scales log-linearly with N . The adaptation to the vertical ULA configuration (with $N = N_V$) is straightforward and not reported here for the sake of brevity.

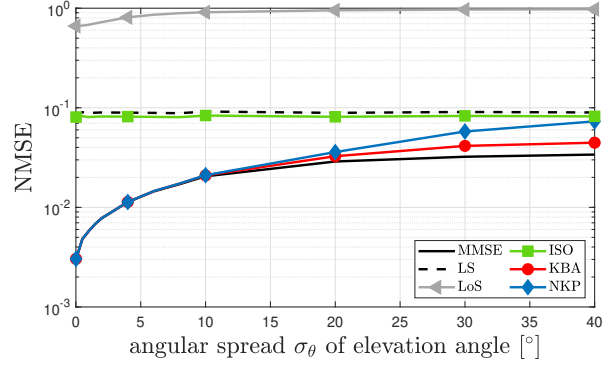


Fig. 4. Average NMSE as a function of the angular spread σ_θ of the elevation angle for the UPA with parameters reported in Table I and $N_H = N_V = 16$. The simulation parameters are those of Table II.

A. DFT-based approximation

If a ULA is used, the covariance matrix \mathbf{R}_k is Hermitian Toeplitz, and it can be approximated with a suitable circulant matrix \mathbf{C}_k [25]–[27], whose first row $\mathbf{c}_k = [c_k(0), c_k(1), \dots, c_k(N-1)]$ is related to the first row $\mathbf{r}_k = [r_k(0), r_k(1), \dots, r_k(N-1)]$ of \mathbf{R}_k by [27]

$$c_k(n) = \begin{cases} r_k(0) & n = 0, \\ \frac{(N-n)r_k(n) + nr_k^*(N-n)}{N} & n = 1, \dots, N-1. \end{cases} \quad (34)$$

Any circulant matrix can be unitarily diagonalized using the discrete Fourier transform (DFT) matrix, i.e., $\mathbf{C}_k = \mathbf{F}\mathbf{\Lambda}_k\mathbf{F}^H$ where $\mathbf{F} = [\mathbf{f}_0 \mathbf{f}_1 \dots \mathbf{f}_{N-1}]$ is the inverse DFT matrix, with $[\mathbf{f}_n]_m = \frac{1}{\sqrt{N}}e^{j2\pi mn/N}$ for $0 \leq m, n \leq N-1$, and $\mathbf{\Lambda}_k$ is the diagonal matrix containing the eigenvalues of \mathbf{C}_k , i.e.,

$$[\mathbf{\Lambda}_k]_{n,n} = \sum_{m=0}^{N-1} c_k(m)e^{-j2\pi mn/N} \quad (35)$$

which are obtained by taking the DFT of the first row of \mathbf{C}_k . Replacing \mathbf{R}_k with \mathbf{C}_k into (9) yields $\hat{\mathbf{h}}_k^{\text{DFT}} = \mathbf{A}_k^{\text{DFT}}\mathbf{y}_k$, with

$$\mathbf{A}_k^{\text{DFT}} = \frac{1}{\tau_p\sqrt{\rho}}\mathbf{F}\mathbf{\Lambda}_k\left(\mathbf{\Lambda}_k + \frac{1}{\gamma}\mathbf{I}_N\right)^{-1}\mathbf{F}^H. \quad (36)$$

We call it the *DFT-based channel estimator*. Its complexity derives from the pre-computation phase, which is $\mathcal{O}(N \log N)$ due to the computation of $\mathbf{\Lambda}_k$ through (35), and from the computation of the matrix-vector product, which is again $\mathcal{O}(N \log N)$, since the DFT matrix \mathbf{F} and its inverse are involved. Hence, the complexity of the DFT-based estimator is $\mathcal{C}_{\text{DFT}} = \mathcal{O}(N \log N)$. Note that, similarly to the KBA case, the DFT-based estimator depends on the true covariance matrix \mathbf{R}_k , which must be estimated as with the MMSE estimator.

B. MMSE analysis

Consider a horizontal ULA, using the relevant parameters listed in Tables I and II. Fig. 5 shows the NMSE in (7) as a function of N . We see that the accuracy of the DFT-based estimator is comparable with the MMSE, and the difference decreases as N increases. This is due to the

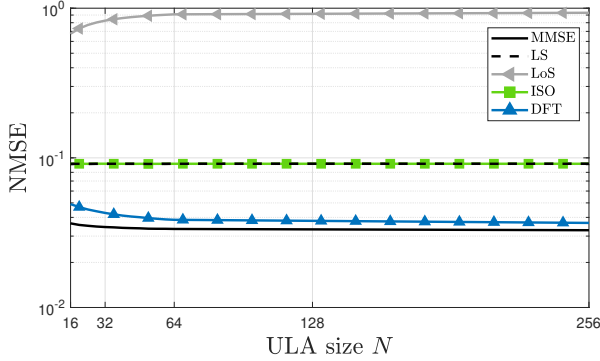


Fig. 5. NMSE as a function of the ULA size N .

fact that the circulant approximation \mathbf{C}_k of the covariance matrix \mathbf{R}_k improves as N grows. Interestingly, the circulant approximation is already quite tight for $N = 64$ (which means $L = N\Delta_H = 3.2$ m). More importantly, this is obtained with a complexity of $\mathcal{O}(N \log N)$, instead of $\mathcal{O}(N^3)$. If $N = 64$, this corresponds to two orders of magnitude of computational saving compared to MMSE. Please refer to [1] for numerical results of vertical ULAs in terms of performance as a function of the ULA size and of the angular spreads.

C. The failure of the combination with KBA

Inspired by the circulant approximation that exploits the Toeplitz structure of \mathbf{R}_k in a ULA, one might be tempted to adopt the same approach for the matrices $\mathbf{R}_{H,k}$ and $\mathbf{R}_{V,k}$ in (24) since they are both Hermitian Toeplitz. This means applying (34) to the first row of either matrix $\mathbf{R}_{H,k}$ or $\mathbf{R}_{V,k}$.

Unfortunately, while the approximation errors for each Hermitian Toeplitz matrix, which can be relevant especially for the off-diagonal elements, appear to be tolerable when implementing the DFT-based scheme (36), this is not true when the approximated versions of the matrices $\mathbf{R}_{H,k}$ or $\mathbf{R}_{V,k}$ are re-combined. In fact, when we apply the Kronecker product to implement the KBA-based approach, the approximation errors get amplified.

To showcase this, Fig. 6 illustrates NSAE_R as a function of σ_θ for the following configurations: ($N_H = N_V = 16$) (solid lines), ($N_H = 1, N_V = 256$) (dashed lines), and ($N_H = 4, N_V = 64$) (dotted lines). We consider $\bar{\varphi} = \bar{\theta} = 0^\circ$, and the scattering of both angles is modeled as Gaussian, with $\sigma_\theta = \sigma_\varphi = 10^\circ$. Red lines with circular markers represent the results by combining the KBA and DFT approaches described above, whereas blue lines with diamond markers report the NKP solution introduced in Sect. IV-A.⁴ As can be seen, keeping the UPA size N constant, the performance gap for all configurations is significant, especially for moderate values of σ_θ , which are of particular interest in practical working conditions. The behavior illustrated in Fig. 6 can be replicated with any set of parameters ($N_H > 1, N_V > 1$).

The impact in terms of channel estimation accuracy can be seen in Fig. 3 (blue curve), which confirms the poor

⁴The curve for the ULA case ($N_H = 1, N_V = 256$) is not reported, as the NKP solution coincides with \mathbf{R}_k , and hence $\text{NSAE} = 0$.

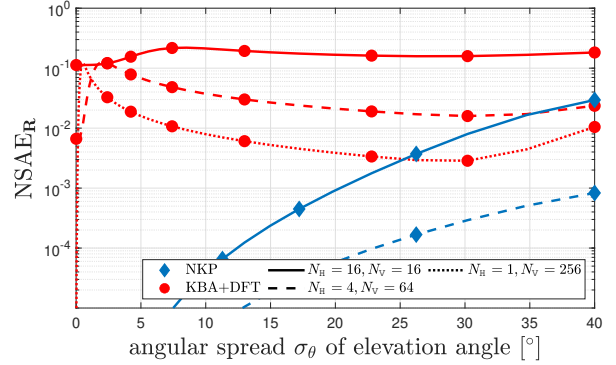


Fig. 6. NSAE of the correlation matrix as a function of the elevation spreading for the combined KBA/DFT approach and the NKP solution.

performance achieved by the KBA/DFT combined method (the accuracy is significantly worse than that achieved by the KBA estimator).

VI. CHANNEL ESTIMATION WITH IMPERFECT KNOWLEDGE OF COVARIANCE MATRICES

So far, we have assumed perfect knowledge of \mathbf{R}_k . This may not be the case in practical scenarios since \mathbf{R}_k changes for various reasons [4]. Measurements suggest that these changes are orders of magnitude slower than the fast variations of the channel [4]. Therefore, it is reasonable to assume that they do not change over $\tau_s = B_s T_s / \tau_c$ blocks [4], where B_s is the system bandwidth, T_s is the timing interval over which the second-order statistics remain unaltered, and τ_c is the length (in samples) of the channel coherence block, that equals the product between the coherence bandwidth and the coherence time of the channel. To quantify τ_s , let us consider a mobile scenario using $B_s = 10$ MHz and $T_s = 0.5$ s [22]. Using $\tau_c = 200$, as considered throughout the paper, which is compatible with a coherence bandwidth of 200 kHz and a coherence time of 1 ms, we get $\tau_s = 25000$.

Suppose the BS has the pilot symbols ϕ_k in $M \leq \tau_s$ coherence blocks. We denote the corresponding observations by $\mathbf{y}_k[1], \dots, \mathbf{y}_k[M]$. An estimate of \mathbf{Q}_k can be obtained by computing the sample correlation matrix given by

$$\hat{\mathbf{Q}}_k^{\text{sample}} = \frac{1}{M} \sum_{m=1}^M \frac{\mathbf{y}_k[m] \mathbf{y}_k^H[m]}{\rho \tau_p^2}. \quad (37)$$

The computation of $\hat{\mathbf{Q}}_k^{\text{sample}}$ requires $\mathcal{O}(MN^2)$ operations, as it involves MN^2 complex multiplications.

A better estimation is typically obtained through matrix regularization by computing the convex combination [4]:

$$\hat{\mathbf{Q}}_k(\eta) = \eta \hat{\mathbf{Q}}_k^{\text{sample}} + (1 - \eta) \hat{\mathbf{Q}}_k^{\text{diag}}, \quad \eta \in [0, 1] \quad (38)$$

where $\hat{\mathbf{Q}}_k^{\text{diag}}$ contains the main diagonal of $\hat{\mathbf{Q}}_k^{\text{sample}}$. The regularization makes $\hat{\mathbf{Q}}_k(\eta)$ a full-rank matrix for any $\eta \in [0, 1)$, and η can be tuned (for example by using numerical methods) to purposely underestimate the off-diagonal elements when

these are considered unreliable. Once $\widehat{\mathbf{Q}}_k(\eta)$ is computed, an estimate of \mathbf{R}_k follows:

$$\widehat{\mathbf{R}}_k(\eta) = \widehat{\mathbf{Q}}_k(\eta) - \frac{1}{\gamma} \mathbf{I}_N \quad (39)$$

which requires only knowledge of γ , i.e., the SNR during the pilot transmission phase.

A. Improved estimation of \mathbf{Q}_k and \mathbf{R}_k

We now develop an improved estimation scheme of the correlation matrix \mathbf{Q}_k that can be used with UPAs. For the ease of notation, we will drop the subscript k from now on.

To accomplish this task, we notice that \mathbf{Q} , analogously to \mathbf{R} , is Hermitian *block*-Toeplitz (and not simply Toeplitz), with $N_V \times N_V$ blocks with size $N_H \times N_H$, i.e.,

$$\mathbf{Q} = \begin{bmatrix} \mathbf{Q}_{1,1} & \mathbf{Q}_{1,2} & \mathbf{Q}_{1,3} & \cdots & \mathbf{Q}_{1,N_V} \\ \mathbf{Q}_{1,2}^H & \mathbf{Q}_{1,1} & \mathbf{Q}_{1,2} & \cdots & \mathbf{Q}_{1,N_V-1} \\ \mathbf{Q}_{1,3}^H & \mathbf{Q}_{1,2}^H & \mathbf{Q}_{1,1} & \cdots & \mathbf{Q}_{1,N_V-2} \\ \vdots & \vdots & \vdots & \ddots & \vdots \\ \mathbf{Q}_{1,N_V}^H & \mathbf{Q}_{1,N_V-1}^H & \mathbf{Q}_{1,N_V-2}^H & \cdots & \mathbf{Q}_{1,1} \end{bmatrix}, \quad (40)$$

where $\mathbf{Q}_{1,j}$ denotes the $N_H \times N_H$ block obtained by \mathbf{Q} as (using MATLAB colon notation)

$$\mathbf{Q}_{1,j} = [\mathbf{Q}]_{1:1:N_H, (j-1)N_H+1:1:N_H}. \quad (41)$$

This means that, due to the block-Toeplitz structure,

$$\mathbf{Q}_{1+j,1+m} = \mathbf{Q}_{1,j} \quad (42)$$

for $j = 1, \dots, N_V - 1$ and $m = 1, \dots, N_V - j$, and that

$$\mathbf{Q}_{j,1} = \mathbf{Q}_{1,j}^H, \quad (43)$$

because of the Hermitian symmetry of the covariance matrix.

To proceed with the estimation, we denote by $\widehat{\mathbf{Q}}_{1,j}$ the estimate of $\mathbf{Q}_{1,j}$ that takes the block-Toeplitz structure (40) into account, by averaging the blocks of $\widehat{\mathbf{Q}}^{\text{sample}}$ over the same (block) diagonal, i.e.:

$$\widehat{\mathbf{Q}}_{1,j} = \frac{1}{N_V - j + 1} \sum_{m=1}^{N_V-j+1} \widehat{\mathbf{Q}}_{m,j+m-1}^{\text{sample}}, \quad (44)$$

for $j = 1, \dots, N_V$, where $\widehat{\mathbf{Q}}_{m,j+m-1}^{\text{sample}}$ is the $N_H \times N_H$ block corresponding to the rows $(m-1)N_H + 1, \dots, mN_H - 1$ and to the columns $(j+m-2)N_H + 1, \dots, (j+m-1)N_H - 1$ of $\widehat{\mathbf{Q}}^{\text{sample}}$ in (37).

It is worth noting that $\mathbf{Q}_{1,j}$ is an $N_H \times N_H$ Toeplitz (but *not* Hermitian) matrix, and we can thus improve the estimation further, by adapting the matrix-based criterion (44) to the elements of $\mathbf{Q}_{1,j}$. In particular, the estimate $\widehat{\mathbf{Q}}_{1,j}^{\text{toe}}$ can be obtained as follows: the first row is computed as

$$\left[\widehat{\mathbf{Q}}_{1,j}^{\text{toe}} \right]_{1,\ell} = \frac{1}{N_H - \ell + 1} \sum_{m=1}^{N_H-\ell+1} \left[\widehat{\mathbf{Q}}_{1,j} \right]_{m,\ell+m-1} \quad (45)$$

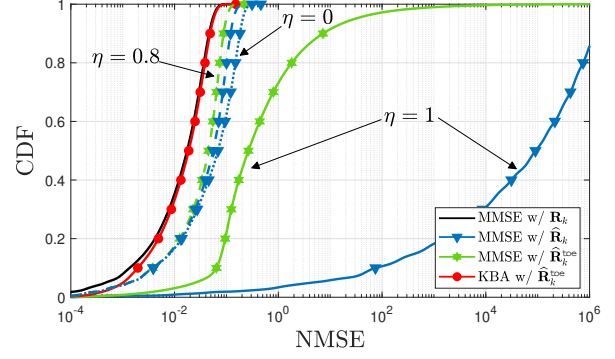


Fig. 7. CDF of the NMSE as a function of the estimation technique using $M = 50$ (black: MMSE with perfect knowledge of \mathbf{R}_k ; red: KBA using $\widehat{\mathbf{R}}_k^{\text{toe}}$ (49); blue: MMSE using $\widehat{\mathbf{R}}_k(\eta)$ (39) in (9) as a function of η ; green: MMSE using $\widehat{\mathbf{R}}_k^{\text{toe}}(\eta)$ (49) in (9) as a function of η).

for $\ell = 1, \dots, N_H$, whereas the first column can be computed as

$$\left[\widehat{\mathbf{Q}}_{1,j}^{\text{toe}} \right]_{\ell,1} = \frac{1}{N_H - \ell + 1} \sum_{m=1}^{N_H-\ell+1} \left[\widehat{\mathbf{Q}}_{1,j} \right]_{\ell+m-1,m} \quad (46)$$

for $\ell = 1, \dots, N_H$. Exploiting the Toeplitz structure, the remaining elements of $\widehat{\mathbf{Q}}_{i,j}^{\text{toe}}$ can be found as

$$\left[\widehat{\mathbf{Q}}_{1,j}^{\text{toe}} \right]_{1+m,\ell+m} = \left[\widehat{\mathbf{Q}}_{1,j}^{\text{toe}} \right]_{1,\ell} \quad (47)$$

$$\left[\widehat{\mathbf{Q}}_{1,j}^{\text{toe}} \right]_{\ell+m,1+m} = \left[\widehat{\mathbf{Q}}_{1,j}^{\text{toe}} \right]_{\ell,1} \quad (48)$$

for $\ell = 1, \dots, N_H - 1$ and $m = 1, \dots, N_H - \ell$.

Once $\mathbf{Q}_{1,j}$ is available for $j = 1, \dots, N_V$, the estimate $\widehat{\mathbf{Q}}^{\text{toe}}$ of the covariance matrix \mathbf{Q} can be found by the same structure as in (40), using $\widehat{\mathbf{Q}}_{1,j}^{\text{toe}}$ instead of $\mathbf{Q}_{1,j}$. An estimate of \mathbf{R} is finally obtained as

$$\widehat{\mathbf{R}}^{\text{toe}} = \widehat{\mathbf{Q}}^{\text{toe}} - \frac{\mathbf{I}_N}{\gamma}. \quad (49)$$

The complexity of the estimator above is mainly due to the computation of $\widehat{\mathbf{Q}}^{\text{sample}}$, and thus is comparable to the one not exploiting the Toeplitz structure, as shown in Sect. VII.

To implement the MMSE estimation scheme, we can replace \mathbf{R} and \mathbf{Q} in (9) with $\widehat{\mathbf{R}}^{\text{toe}}$ and $\widehat{\mathbf{Q}}^{\text{toe}}$, respectively. We can also adopt the KBA- and the DFT-based methods, for the UPA and ULA cases, respectively, by considering $\widehat{\mathbf{R}}^{\text{toe}}$ in (24) and (34), instead of \mathbf{R} .

B. Performance analysis

We now evaluate the accuracy of the different estimators, using the system setup detailed in Table II, assuming a square UPA with parameters listed in Table I. Fig. 7 reports the cumulative distribution function (CDF) of NMSE in (7) assuming that $M = 50$ observations are used for the estimation of the channel covariance matrix. In particular, the red line with circular markers corresponds to the KBA estimator that uses $\widehat{\mathbf{R}}_k^{\text{toe}}$ in (49), whereas blue and green lines correspond to the MMSE estimator when using (39) and (49),

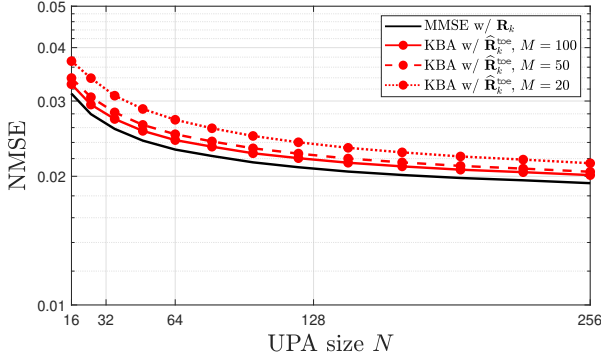


Fig. 8. NMSE as a function of the size N (square UPA, with $N_H = N_V$) with imperfect statistical knowledge (KBA-based estimator).

respectively. Solid, dashed, and dotted lines report the results obtained with the regularization parameter η introduced in (38) with values $\{1, 0.8, 0\}$, respectively.⁵ For comparison, we also report the NMSE achieved by the MMSE estimator with perfect knowledge of \mathbf{R}_k (black line).

The KBA estimator performs close to the MMSE estimator with perfect knowledge of channel statistics, whereas the MMSE estimator with imperfect knowledge of channel statistics shows a gap that depends on η , and thus confirming the benefits yielded by the regularization technique (38). Note also that the MMSE estimator using (49) outperforms the one using (39). For this reason, in the remainder of the paper, we will adopt (49) with a regularization factor $\eta = 0.8$.⁶ Additional simulations, not reported for the sake of clarity, show that: *i*) regularizing the KBA estimator does *not* provide additional benefits, as the performance is already tight to the optimal one; and *ii*) using (39) instead of (49) produces poorer performance of the KBA estimator. Hence, in the remainder of the paper we will use (49) when considering KBA.

Fig. 8 reports the average as a function of the size N for a square UPA, obtained by averaging over all possible UE positions in the system setup detailed in Table II. As can be seen, an estimation accuracy comparable to that obtained with perfect knowledge of \mathbf{R}_k is already achieved with $M = 20$. Similar trends are observed for different array sizes and/or scattering scenarios. The results concerning ULA configurations are reported in [1].

VII. COMPLEXITY ANALYSIS

Next, we assess the computational burden in terms of complex operations (additions and/or multiplications), required by the *entire* channel estimation procedure of the investigated estimators. Without loss of generality, next we consider $N_H \geq N_V$. The analysis can be simply extended to the case $N_H < N_V$.

⁵In the case of the MMSE estimator using (49), the same regularization method (38) is applied to the matrix $\hat{\mathbf{Q}}_k^{\text{toe}}$. Note that, for $\eta = 0$, the two methods coincide, and only the lower triangles is reported.

⁶The optimal η does depend on the network setup and the UPA parameters, including size and spacing.

Table III
COMPLEXITY OF CHANNEL ESTIMATION SCHEMES.

Scheme	$\hat{\mathbf{Q}}_k^{\text{toe}}$	\mathbf{A}_k	$\mathbf{A}_k \mathbf{y}_k$
LS	–	–	$\mathcal{O}(N)$
LoS	–	–	$\mathcal{O}(N)$
ISO	–	–	$\mathcal{O}(N^2)$
MMSE	$\mathcal{O}(MN^2)$	$\mathcal{O}(N^2 N_V)$	$\mathcal{O}(N^2)$
KBA	$\mathcal{O}(MN^2)$	$\mathcal{O}(N_H^3)$	$\mathcal{O}((N_H + N_V)N)$
DFT	$\mathcal{O}(N^2)$	$\mathcal{O}(N \log N)$	$\mathcal{O}(N \log N)$

A. Computation of $\hat{\mathbf{Q}}_k^{\text{toe}}$

From (44), the calculation of $\hat{\mathbf{Q}}_{1,j}$, for $j = 1, \dots, N_V$, requires a total of approximately $N^2/2$ additions and $N_H N$ multiplications. Analogously, the evaluation of $\hat{\mathbf{Q}}_{1,j}^{\text{toe}}$ in (45), with $j = 1, \dots, N_V$, requires a total of $NN_H/2$ additions and N multiplications. Thanks to Toeplitz-block Toeplitz structure, the computation of $\hat{\mathbf{Q}}_k^{\text{toe}}$ has a complexity order of $\mathcal{O}(MN^2 + N^2/2 + N_H N) \approx \mathcal{O}(MN^2)$. No additional complexity is incurred compared to the unstructured $\hat{\mathbf{Q}}_k^{\text{sample}}$.

B. Computation of matrix \mathbf{A}_k via $\hat{\mathbf{R}}_k^{\text{toe}}$ and $\hat{\mathbf{Q}}_k^{\text{toe}}$

The MMSE estimator is characterized by the matrix

$$\hat{\mathbf{A}}_k^{\text{MMSE}} = \frac{1}{\tau_p \sqrt{\rho}} \hat{\mathbf{R}}_k^{\text{toe}} (\hat{\mathbf{Q}}_k^{\text{toe}})^{-1} \quad (50)$$

obtained from (9) by replacing the true covariance matrix \mathbf{R}_k with its estimate $\hat{\mathbf{R}}_k^{\text{toe}}$. Once $\hat{\mathbf{Q}}_k^{\text{toe}}$ is available, $\hat{\mathbf{R}}_k^{\text{toe}}$ can easily be obtained through (49) with N additions. As for the computation of $(\hat{\mathbf{Q}}_k^{\text{toe}})^{-1}$, an efficient algorithm for the inversion of a Toeplitz-block Toeplitz matrix can be found in [33]. It has a complexity $\mathcal{O}(N^2 N_V)$. The maximum complexity occurs for square UPAs, where $N_H = N_V = \sqrt{N}$, resulting in $\mathcal{O}(N^{2.5})$.

The KBA estimator is obtained by approximating $\hat{\mathbf{R}}_k^{\text{toe}}$ with the Kronecker product $\hat{\mathbf{R}}_{V,k}^{\text{toe}} \otimes \hat{\mathbf{R}}_{H,k}^{\text{toe}}$. The matrix $\hat{\mathbf{A}}_k^{\text{KBA}}$ is derived from (18) by replacing

$$\mathbf{K}_1 = \mathbf{U}_1 \mathbf{\Lambda}_1 \mathbf{U}_1^H \quad (51)$$

$$\mathbf{K}_2 = \mathbf{U}_2 \mathbf{\Lambda}_2 \mathbf{U}_2^H \quad (52)$$

with

$$\hat{\mathbf{R}}_{V,k}^{\text{toe}} = \hat{\mathbf{U}}_{V,k}^{\text{toe}} \hat{\mathbf{\Lambda}}_{V,k}^{\text{toe}} (\hat{\mathbf{U}}_{V,k}^{\text{toe}})^H \quad (53)$$

$$\hat{\mathbf{R}}_{H,k}^{\text{toe}} = \hat{\mathbf{U}}_{H,k}^{\text{toe}} \hat{\mathbf{\Lambda}}_{H,k}^{\text{toe}} (\hat{\mathbf{U}}_{H,k}^{\text{toe}})^H \quad (54)$$

respectively. By utilizing the algorithm proposed in [34], the computation of (53) and (54) has a complexity of $\mathcal{O}(N_H^3)$ and $\mathcal{O}(N_V^3)$, respectively. Consequently, the factorization of $\hat{\mathbf{A}}_k^{\text{KBA}}$ can be achieved with a complexity of $\mathcal{O}(N_H^3)$, which amounts to $\mathcal{O}(N^{1.5})$ for square UPAs.

C. Computation of channel estimate $\hat{\mathbf{h}}_k$

All estimation schemes are *linear* of the form given in (6), based on \mathbf{y}_k . The complexity associated with the computation of \mathbf{y}_k is $\mathcal{O}(N)$, since it requires $(\tau_p - 1)N$ complex sums and $\tau_p N$ complex products.

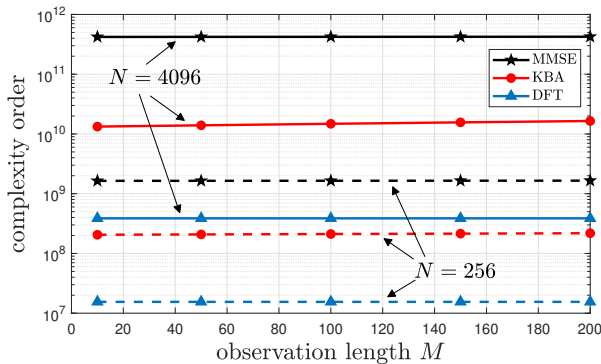


Fig. 9. Complexity order as a function of the observation length for different estimation schemes and array sizes ($\tau_s = 25,000$).

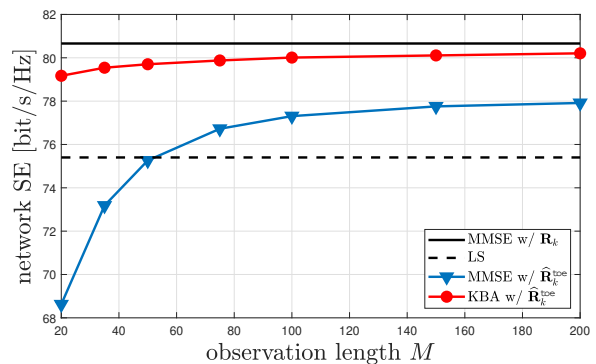
The LS estimator simply multiplies \mathbf{y}_k and the real diagonal matrix in (11). Accordingly, it has an overall complexity $\mathcal{O}(N)$. The MMSE estimator multiplies \mathbf{y}_k by the matrix (50). From the Appendix, it follows that it exhibits a computational complexity of $\mathcal{O}(N^2)$. This is because computing $(\hat{\mathbf{Q}}_k^{\text{toe}})^{-1}\mathbf{y}_k$ requires N^2 multiplications and (approximately) N^2 additions, and the same number of operations is needed to compute $\hat{\mathbf{R}}_k^{\text{toe}}(\hat{\mathbf{Q}}_k^{\text{toe}})^{-1}\mathbf{y}_k$.

The KBA scheme makes use of the matrix $\hat{\mathbf{A}}_k^{\text{KBA}}$. From the Appendix, based on (18) and exploiting the structure of KBA due to the Kronecker products, the complexity associated with the computation of $\hat{\mathbf{A}}_k^{\text{KBA}}\mathbf{y}_k$ is $\mathcal{O}((N_H + N_V)N)$. If $N_H = N_V = \sqrt{N}$, the complexity is $\mathcal{O}(N\sqrt{N})$.

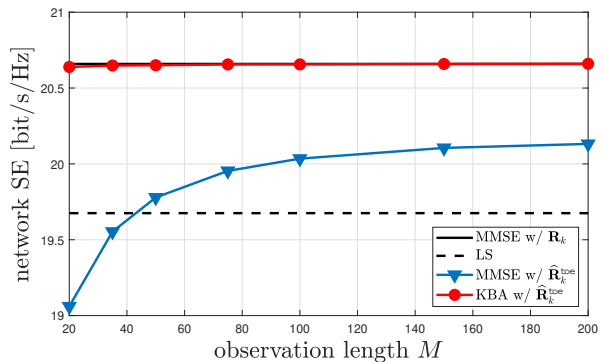
D. Summary

The above results are summarized in Table III, which also contains the complexity for the DFT-based method derived in Sect. V (please refer to [1] for more details on the complexity associated to this technique). Each column contains the complexity associated to each of the three phases in the channel estimation process. Based on the considerations in Sect. VI, the second-order statistics of the channel remain unchanged for τ_s channel coherence blocks, which means that the first two operations (i.e., estimation of $\hat{\mathbf{Q}}^{\text{toe}}$ and $\hat{\mathbf{A}}_k$) need to be performed only *once per* τ_s channel realizations, while the third operation (estimation of $\hat{\mathbf{A}}_k\mathbf{y}_k$) is needed for each channel realizations. As a consequence, the whole estimation process has a complexity order given by the sum of the complexity due to $\hat{\mathbf{Q}}^{\text{toe}}$, plus the one due to $\hat{\mathbf{A}}_k$, plus τ_s times the one due to $\hat{\mathbf{A}}_k\mathbf{y}_k$. Using Table III, this means that the complexity order is $\mathcal{O}(MN^2 + N^2N_V + \tau_s N^2)$ for the MMSE, and $\mathcal{O}(MN^2 + N_H^3 + \tau_s(N_H + N_V)N)$ for the KBA. Assuming a square array, in which $N_H = N_V = \sqrt{N}$, the complexity orders become $\mathcal{O}((M + \sqrt{N} + \tau_s)N^2)$ and $\mathcal{O}((MN + \sqrt{N} + 2\tau_s\sqrt{N})N)$, respectively.

To better illustrate the impact of the UPA size on the computational burden, Fig. 9 reports the complexity as a function of the observation length M , using $N = 256$ (dashed lines) and $N = 4096$ (solid lines), considering $\tau_s = 25,000$. As can be seen, the gap between the MMSE estimator (black lines) and the KBA scheme (red lines) is already an order of magnitude for relatively small UPAs ($N = 256$), while it



(a) RZF combining.



(b) MR combining.

Fig. 10. Sum-SE as a function of the observation length M with RZF and MF! combining.

becomes more significant for larger UPAs ($N = 4096$), and keeps increasing with N . Note that, in highly time-varying scenarios, characterized by large values of τ_s (as the channel coherence time decreases faster than T_s), the gap increases. The same conclusions hold for other UPA shapes other than the square one.

Fig. 9 also reports the complexity required by a ULA with the same number of antennas (note that, based on Table III, the complexity does not depend on M). The computational saving is even more significant, at the cost of a less compact array size and a reduced capability to capture variations in both azimuth and elevation planes.

VIII. UPLINK SPECTRAL EFFICIENCY EVALUATION

Channel estimation is the ancillary task to support data detection, which is the ultimate goal of a communication system. Hence, we now compare the investigated solutions in terms of achievable uplink SE. This is obtained with the well-known use-and-then-forget bound [2, Sect. 4.2], which yields

$$\underline{\text{SE}}_k = \left(1 - \frac{\tau_p}{\tau_c}\right) \mathbb{E} \left\{ \log_2 \left(1 + \underline{\gamma}_k\right) \right\} \quad [\text{bit/s/Hz}], \quad (55)$$

where the factor τ_p/τ_c accounts for the fraction of samples per coherence block used for channel estimation, with τ_c being the

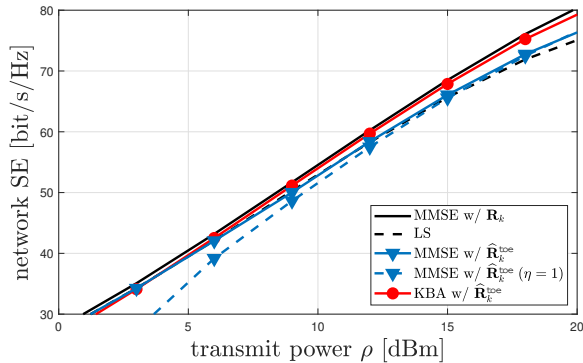


Fig. 11. Sum-SE with RZF as a function of the transmit power ρ in dBm.

length of each coherence block, and $\underline{\gamma}_k$ is given by

$$\frac{|\mathbb{E}\{\mathbf{v}_k^H \mathbf{h}_k\}|^2}{\sum_{i=1}^K \mathbb{E}\{|\mathbf{v}_k^H \mathbf{h}_i|^2\} - |\mathbb{E}\{\mathbf{v}_k^H \mathbf{h}_k\}|^2 + \frac{\sigma^2}{\rho} \mathbb{E}\{\|\mathbf{v}_k\|^2\}}, \quad (56)$$

with $\mathbf{v}_k \in \mathbb{C}^N$ being the receive combining vector associated to UE k . Notice that the expectations are computed with respect to all sources of randomness. We consider both regularized zero forcing (RZF) combining, according to which

$$\mathbf{v}_k = \left(\sum_{i=1}^K \hat{\mathbf{h}}_i \hat{\mathbf{h}}_i^H + \frac{\sigma^2}{\rho} \mathbf{I}_N \right)^{-1} \hat{\mathbf{h}}_k \quad (57)$$

and maximum ratio (MR) combining $\mathbf{v}_k = \hat{\mathbf{h}}_k$.

Fig. 10 shows the network SE, given by

$$\underline{\text{SE}} = \sum_{k=1}^K \underline{\text{SE}}_k \quad [\text{bit/s/Hz}] \quad (58)$$

as a function of the observations M used to estimate the channel statistics. The RZF combining scheme (57) is used in Fig. 10(a), while MR is adopted in Fig. 10(b). The network parameters are detailed in Tables I and II, with $K = 10$ randomly placed UEs. The black solid line corresponds to the MMSE estimator using perfect knowledge of the channel statistics \mathbf{R}_k for both the combining and the estimation schemes (i.e., the estimation makes use of true \mathbf{R}_k), whereas the black dashed line depicts the results using the LS estimator (11); blue and red lines correspond to the results obtained assuming *imperfect* channel statistics for the MMSE and the KBA methods, respectively, and thus $\hat{\mathbf{R}}_k$ (used for both estimation and combining) is estimated using the methods introduced in Sect. VI: more in detail, the MMSE estimator uses (39) with $\eta = 0.8$, whereas the KBA-based estimator uses (49) (*without* any regularization parameter η).

We notice that, while the gap between the imperfect-knowledge MMSE estimator (blue line) and the benchmark curves remains significant even for large values of M , the performance of the KBA-based scheme (red line) is very close to the optimal one (black curve), even for moderately low values of M (for MR combining, there is no difference, whereas the RZF shows some gap, yet much smaller than that provided by the MMSE estimator with imperfect knowledge,

and decreasing with M). This confirms the results presented in Sect. VI-B, in which the KBA-based method, thanks to a simpler structure, introduces more robustness compared to the MMSE counterpart for the same observation length M , and makes it more suitable for more dynamic scenarios, in which the coherence time is reduced (and hence M needs to be kept as low as possible). In addition, the KBA-based method does not call for any numerical optimization of the regularization parameter η (unlike the MMSE estimator – see comments to Fig. 7), and it can thus be universally adopted, irrespectively of the network setup (including UPA parameters).

Fig. 11 shows the network SE with RZF as a function of the transmit power ρ . The network setup is identical to the one considered for Fig. 10(a), assuming $M = 50$ channel observations for the covariance matrix estimation task. As can be seen, when $\rho = 20$ dBm (i.e., the same parameter setup considered for Fig. 10(a)), the KBA-based method outperforms the MMSE one by 4.5 bit/s/Hz.⁷ Only when increasing ρ , in particular when $\rho \geq 28$ dBm (not reported here in the figure), in this simulation setup the two methods provide approximately the same performance. This means that the proposed KBA method is particularly suitable in low-SNR regimes, in which the link budget does not guarantee sufficient accuracy for the MMSE counterpart. Similar trends, not reported here for the sake of brevity, are observed for MR combining.

IX. CONCLUSION

We developed channel estimation schemes for large-scale MIMO systems that achieve accuracy levels comparable to the optimal MMSE estimator, while also offering reduced complexity and enhanced robustness to the imperfect knowledge of channel statistics. Both UPAs and ULAs were studied. In the case of UPAs, we exploited the inherent structure of the spatial correlation matrix to approximate it by a Kronecker product, and in the case of ULAs, we used a circulant approximation to further reduce the computational complexity. Comparisons were made with the optimal MMSE estimator and other alternatives with less complexity (e.g., the LS estimator). Numerical results confirmed the effectiveness of the proposed methods in terms of UL SE with various combining schemes, approaching MMSE performance while significantly reducing computational complexity. Specifically, the computational load scales as $N\sqrt{N}$ and $N \log N$ for squared planar arrays and linear arrays, respectively. Furthermore, the proposed schemes exhibited improved robustness in scenarios with imperfect channel statistics and low-to-medium SNR scenarios. Future extensions of the proposed methodology may consider different shapes for the array (e.g., cylindrical), and the impact of near-field propagation conditions, which become relevant as the array size increases and/or the carrier frequency increases (e.g., see [15], [35]).

⁷Note that the optimal regularization factor η is a function of all simulation parameters, including ρ , and thus changes point by point – this is the reason why the solid lines is always higher than the dashed line, without regularization.

APPENDIX

The estimation of \mathbf{h}_k calls for the product between \mathbf{A}_k and \mathbf{y}_k . Accordingly, when \mathbf{A}_k is written as a product of matrices (as occurs, for instance, with the MMSE or the KBA estimators), it is convenient not to perform the products. Indeed, assume that we have to compute $\mathbf{B}_1\mathbf{B}_2\mathbf{b}$, where \mathbf{B}_1 and \mathbf{B}_2 are $N \times N$ matrices and \mathbf{b} is an N -dimensional vector. If we first multiply \mathbf{B}_1 and \mathbf{B}_2 , and then the resulting matrix and \mathbf{b} , we have to perform $N^3 + N^2$ multiplications and $(N-1)N^2 + (N-1)N$ additions. On the other hand, if we first compute the product between \mathbf{B}_2 and \mathbf{b} , and then the product between \mathbf{B}_1 and the resulting vector, $2N^2$ multiplications and $2(N-1)N$ additions are needed. This means, for example, that when considering the MMSE estimator it is better to compute first $(\hat{\mathbf{Q}}_k^{\text{toe}})^{-1}\mathbf{y}_k$ and then $\hat{\mathbf{R}}_k^{\text{toe}} \left[(\hat{\mathbf{Q}}_k^{\text{toe}})^{-1}\mathbf{y}_k \right]$. An analogous approach can be conveniently used with the KBA estimator. Another useful result, that can be exploited to reduce the complexity of the KBA estimator, concerns the computation of the product $(\mathbf{C}_1 \otimes \mathbf{C}_2)\mathbf{b}$, where \mathbf{C}_1 is $m \times m$, \mathbf{C}_2 is $n \times n$, and \mathbf{b} is an mn -dimensional vector. The evaluation of $(\mathbf{C}_1 \otimes \mathbf{C}_2)\mathbf{b}$ can efficiently be performed with $(m+n)mn$ floating-point operations instead of m^2n^2 [36].

REFERENCES

- [1] A. A. D'Amico, G. Bacci, and L. Sanguinetti, "DFT-based channel estimation for holographic MIMO," in *Proc. Asilomar Conf. Signals, Systems, and Computers*, Pacific Grove, CA, Oct.-Nov. 2023.
- [2] E. Björnson, J. Hoydis, and L. Sanguinetti, "Massive MIMO networks: Spectral, energy, and hardware efficiency," *Foundations and Trends® in Signal Processing*, vol. 11, no. 3-4, pp. 154–655, 2017.
- [3] E. Björnson, L. Sanguinetti, H. Wymeersch, J. Hoydis, and T. L. Marzetta, "Massive MIMO is a reality – What is next?" *Digit. Signal Process.*, vol. 94, no. C, pp. 3–20, nov 2019. [Online]. Available: <https://doi.org/10.1016/j.dsp.2019.06.007>
- [4] L. Sanguinetti, E. Björnson, and J. Hoydis, "Toward massive MIMO 2.0: Understanding spatial correlation, interference suppression, and pilot contamination," *IEEE Trans. Commun.*, vol. 68, no. 1, pp. 232–257, 2020.
- [5] Z. Wang, J. Zhang, H. Du, W. E. I. Sha, B. Ai, D. Niyato, and M. Debbah, "Extremely large-scale MIMO: Fundamentals, challenges, solutions, and future directions," *IEEE Wireless Communications*, vol. 31, no. 3, pp. 1–9, 2023.
- [6] E. Björnson, C.-B. Chae, R. W. Heath, T. L. Marzetta, A. Mezghani, L. Sanguinetti, F. Rusek, M. R. Castellanos, D. Jun, and O. T. Demir, "Towards 6G MIMO: Massive spatial multiplexing, dense arrays, and interplay between electromagnetics and processing," 2024.
- [7] J. An, C. Yuen, C. Huang, M. Debbah, H. V. Poor, and L. Hanzo, "A tutorial on holographic MIMO communications – part I: Channel modeling and channel estimation," *IEEE Commun. Letters*, vol. 27, no. 7, pp. 1664–1668, 2023.
- [8] J. An, C. Xu, L. Gan, and L. Hanzo, "Low-complexity channel estimation and passive beamforming for RIS-assisted MIMO systems relying on discrete phase shifts," *IEEE Trans. Commun.*, vol. 70, no. 2, pp. 1245–1260, 2022.
- [9] Y. Liu, Z. Tan, H. Hu, L. J. Cimini, and G. Y. Li, "Channel estimation for OFDM," *IEEE Commun. Surv. Tut.*, vol. 16, no. 4, pp. 1891–1908, 2014.
- [10] F. Dai and J. Wu, "Efficient broadcasting in ad hoc wireless networks using directional antennas," *IEEE Trans. Parallel Distrib. Syst.*, vol. 17, no. 4, pp. 335–347, 2006.
- [11] Z. Xiao, T. He, P. Xia, and X.-G. Xia, "Hierarchical codebook design for beamforming training in millimeter-wave communication," *IEEE Trans. Wireless Commun.*, vol. 15, no. 5, pp. 3380–3392, 2016.
- [12] J. Zhang, Y. Huang, Q. Shi, J. Wang, and L. Yang, "Codebook design for beam alignment in millimeter wave communication systems," *IEEE Trans. Commun.*, vol. 65, no. 11, pp. 4980–4995, 2017.
- [13] S. Noh, M. D. Zoltowski, and D. J. Love, "Multi-resolution codebook and adaptive beamforming sequence design for millimeter wave beam alignment," *IEEE Trans. Wireless Commun.*, vol. 16, no. 9, pp. 5689–5701, 2017.
- [14] Z. Wan, Z. Gao, F. Gao, M. Di Renzo, and M.-S. Alouini, "Terahertz massive MIMO with holographic reconfigurable intelligent surfaces," *IEEE Trans. Commun.*, vol. 69, no. 7, pp. 4732–4759, 2021.
- [15] M. Cui and L. Dai, "Channel estimation for extremely large-scale MIMO: Far-field or near-field?" *IEEE Trans. Commun.*, vol. 70, no. 4, pp. 2663–2677, 2022.
- [16] M. Ghermezcheshmeh and N. Zlatanov, "Parametric channel estimation for LoS dominated holographic massive MIMO systems," *IEEE Access*, pp. 44 711–44 724, 2023.
- [17] Q. Qin, G. Lin, P. Cheng, and B. Gong, "Time-varying channel estimation for millimeter wave multiuser MIMO systems," *IEEE Trans. Veh. Technol.*, p. 9435–9448, 2018.
- [18] L. Cheng, G. Yue, X. Xiong, Y. Liang, and S. Li, "Tensor decomposition-aided time-varying channel estimation for millimeter wave MIMO systems," *IEEE Wireless Commun. Lett.*, pp. 1216–1219, 2019.
- [19] J. Zhang, D. Rakhimov, and M. Haardt, "Gridless channel estimation for hybrid mmWave MIMO systems via tensor-ESPRIT algorithms in DFT beamspace," *IEEE J. Sel. Topics Signal Process.*, pp. 816–831, 2021.
- [20] Ö. T. Demir, E. Björnson, and L. Sanguinetti, "Channel modeling and channel estimation for holographic massive MIMO with planar arrays," *IEEE Wireless Commun. Lett.*, vol. 11, no. 5, pp. 997–1001, 2022.
- [21] A. Pizzo, L. Sanguinetti, and T. L. Marzetta, "Fourier plane-wave series expansion for holographic MIMO communications," *IEEE Trans. Wireless Commun.*, vol. 21, no. 9, pp. 6890–6905, 2022.
- [22] E. Björnson, L. Sanguinetti, and M. Debbah, "Massive MIMO with imperfect channel covariance information," in *Proc. Asilomar Conf. Signals, Systems and Computers*, Pacific Grove, CA, USA, 2016, pp. 974–978.
- [23] C. Van Loan and N. Pitsianis, "Approximation with Kronecker products," in *Linear Algebra for Large Scale and Real Time Applications*. M. S. Moonen and G. H. Golub, Eds. Dordrecht, The Netherlands: Kluwer Publications, 1992, pp. 293–314.
- [24] C. F. Van Loan, "The ubiquitous Kronecker product," *J. Computational and Applied Mathematics*, vol. 123, pp. 85–100, 2000.
- [25] J. Pearl, "Basis-restricted transformations and performance measures for spectral representations (corresp.)," *IEEE Trans. Information Theory*, vol. 17, no. 6, pp. 751–752, 1971.
- [26] —, "On coding and filtering stationary signals by discrete fourier transforms (corresp.)," *IEEE Trans. Information Theory*, vol. 19, no. 2, pp. 229–232, 1973.
- [27] Z. Zhu and M. B. Wakin, "On the asymptotic equivalence of circulant and Toeplitz matrices," *IEEE Trans. Information Theory*, vol. 63, no. 5, pp. 2975–2992, 2017.
- [28] E. Björnson and L. Sanguinetti, "Rayleigh fading modeling and channel hardening for reconfigurable intelligent surfaces," *IEEE Wireless Commun. Letters*, vol. 10, no. 4, pp. 830–834, 2021.
- [29] A. Sayeed, "Deconstructing multiantenna fading channels," *IEEE Trans. Signal Process.*, vol. 50, no. 10, pp. 2563–2579, 2002.
- [30] A. F. Molisch, *Wireless Communications: From Fundamentals to Beyond 5G*, 3rd ed. West Sussex, UK: J. Wiley & Sons, 2022.
- [31] R. Zhang, X. Lu, J. Zhao, L. Cai, and J. Wang, "Measurement and modeling of angular spreads of three-dimensional urban street radio channels," *IEEE Trans. Veh. Technol.*, pp. 3555–3570, 2017.
- [32] G. Bacci, L. Sanguinetti, and E. Björnson, "Spherical wavefronts improve MU-MIMO spectral efficiency when using electrically large arrays," *IEEE Wireless Commun. Letters*, vol. 12, no. 17, pp. 1219–1223, 2023.
- [33] M. Wax and T. Kailath, "Efficient inversion of Toeplitz-block Toeplitz matrix," *IEEE Trans. Acoustics, Speech, and Signal Process.*, vol. 31, no. 5, pp. 1218–1221, 1983.
- [34] F. W. Trench, "Numerical solution of the eigenvalue problem for Hermitian Toeplitz matrices," *SIAM J. Matrix Analysis and Applications*, vol. 10, no. 2, pp. 135–146, 1989.
- [35] C. Huang, J. Xu, W. Xu, X. You, C. Yuen, and Y. Chen, "Low-complexity channel estimation for extremely large-scale MIMO in near field," *IEEE Wireless Commun. Lett.*, p. 671–675, 2024.
- [36] T. Dayar and M. C. Orhan, "On vector-kronecker product multiplication with rectangular factors," *SIAM J. Scientific Computing*, vol. 37, no. 5, pp. S526–S543, 2015. [Online]. Available: <https://doi.org/10.1137/140980326>



Giacomo Bacci (Senior Member, IEEE) received the Ph.D. degree in information engineering from the University of Pisa, Pisa, Italy, in 2008. From 2006 to 2007, he was a visiting student research collaborator with Princeton University, Princeton, NJ, USA. From 2008 to 2014, he was a post-doctoral research fellow with the University of Pisa. From 2008 to 2012, he was also a software engineer with Wiser Srl, Livorno, Italy, and from 2012 to 2014, he was also enrolled as a visiting post-doctoral research associate with Princeton University. From

2015 to 2021, he was a product manager for interactive satellite broadband communications at MBI Srl, Pisa, Italy. Since 2022, he joined the University of Pisa as a tenure-track assistant professor.

Dr. Bacci is the recipient of the FP7 Marie Curie International Outgoing Fellowships for career development (IOF) 2011 GRAND-CRU, the Best Paper Award from the IEEE Wireless Communications and Networking Conference (WCNC) in 2013, the Best Student Paper Award from the International Waveform Diversity and Design Conference (WDD) in 2007, the Best Session Paper at the ESA Workshop on EGNOS Performance and Applications in 2005, and the 2014 URSI Young Scientist Award. He is currently serving as an associate editor for IEEE Communications Letters and EURASIP Journal on Advances in Signal Processing and he is a Senior Member of the IEEE and a Senior Member of the International Union of Radio Science.



Antonio A. D'Amico (Senior Member, IEEE) received the Laurea degree in Electronic Engineering in 1992 and the Ph.D. degree in 1997, both from the University of Pisa, Italy. He is currently an Associate Professor in the "Dipartimento di Ingegneria dell'Informazione" of the University of Pisa, Italy. His research interests are in digital communication theory and statistical signal processing, with emphasis on synchronization algorithms, channel estimation, localization, and detection algorithms.

He is currently serving as an Associate Editor for the IEEE Transactions on Wireless Communications.



Luca Sanguinetti (Senior Member, IEEE) received the Laurea degree (cum laude) in Telecommunications Engineering and the Ph.D. degree in information engineering from the University of Pisa, Italy, in 2002 and 2005, respectively. In 2004, he was a visiting Ph.D. student at the German Aerospace Center (DLR), Oberpfaffenhofen, Germany. During the period June 2007 - June 2008, he was a post-doctoral associate in the Dept. Electrical Engineering at Princeton, NJ, USA. From July 2013 to October 2017 he was with Large Systems and Networks

Group (LANEAS), CentraleSupélec, France. He is currently a Full Professor in the "Dipartimento di Ingegneria dell'Informazione" of the University of Pisa, Italy.

He served as an Associate Editor for IEEE TRANSACTIONS ON COMMUNICATIONS, IEEE TRANSACTIONS ON WIRELESS COMMUNICATIONS and IEEE SIGNAL PROCESSING LETTERS, and as Lead Guest Editor of IEEE JOURNAL ON SELECTED AREAS OF COMMUNICATIONS Special Issue on "Game Theory for Networks" and as an Associate Editor for IEEE JOURNAL ON SELECTED AREAS OF COMMUNICATIONS (series on Green Communications and Networking). Dr. Sanguinetti is currently a member of the Executive Editorial Committee of IEEE TRANSACTIONS ON WIRELESS COMMUNICATIONS.

His expertise and general interests span the areas of communications and signal processing. Dr. Sanguinetti co-authored the textbooks *Massive MIMO Networks: Spectral, Energy, and Hardware Efficiency* (2017) and *Foundations on User-centric Cell-free Massive MIMO* (2020). He received the 2018 and 2022 Marconi Prize Paper Award in Wireless Communications, the 2023 IEEE Communications Society Outstanding Paper Award.